Full Length Article

Fe/SSZ-13 as an NH₃-SCR catalyst: A reaction kinetics and FTIR/Mössbauer spectroscopic study

Feng Gao [a,*], Márton Kollár [a], Ravi K. Kukkadapu [b], Nancy M. Washton [b], Yilin Wang [a], János Szanyi [a,*], Charles H.F. Peden [a,*]

[a] Institute for Integrated Catalysis, Pacific Northwest National Laboratory, P.O. Box 999, Richland, WA 99352, United States
[b] Environmental Molecular Sciences Laboratory, Pacific Northwest National Laboratory, P.O. Box 999, Richland, WA 99352, United States

A B S T R A C T

Using a traditional aqueous solution ion-exchange method under a protecting atmosphere of N_2, an Fe/SSZ-13 catalyst active in NH₃-SCR was synthesized. Mössbauer and FTIR spectroscopies were used to probe the nature of the Fe sites. In the fresh sample, the majority of Fe species are extra-framework cations. The likely monomeric and dimeric ferric ions in hydrated form are $[Fe(OH)_2]^+$ and $[HO-Fe-O-Fe-OH]^{2+}$, based on Mössbauer measurements. During the harsh hydrothermal aging (HTA) applied in this study, a majority of cationic Fe species convert to $FeAlO_x$ and clustered FeO_x species, accompanied by dealumination of the SSZ-13 framework. The clustered FeO_x species do not give a sextet Mössbauer spectrum, indicating that these are highly disordered. However, some Fe species in cationic positions remain after aging as determined from Mössbauer measurements and CO/NO FTIR titrations. NO/NH₃ oxidation reaction tests reveal that dehydrated cationic Fe is substantially more active in catalyzing oxidation reactions than the hydrated ones. For NH₃-SCR, enhancement of NO oxidation under 'dry' conditions promotes SCR rates below ~300 °C. This is due mainly to contribution from the "fast" SCR channel. Above ~300 °C, enhancement of NH₃ oxidation under 'dry' conditions, however, becomes detrimental to NO_x conversions. The HTA sample loses much of the SCR activity below ~300 °C; however, above ~400 °C much of the activity remains. This may suggest that the $FeAlO_x$ and FeO_x species become active at such elevated temperatures. Alternatively, the high-temperature activity may be maintained by the remaining extra-framework cationic species. For potential practical applications, Fe/SSZ-13 may be used as a co-catalyst for Cu/CHA as integral aftertreatment SCR catalysts on the basis of the stable high temperature activity after hydrothermal aging.

Published by Elsevier B.V.

1. Introduction

For the last two decades or so, the catalysis community has been addressing the significant challenge of reducing NO_x under the highly oxidizing (*lean-burn*) conditions encountered in the exhaust of diesel-powered vehicles. NO_x storage-reduction (NSR) and selective catalytic reduction (SCR) are leading NO_x emission control techniques for such lean-burn diesel engines [1–6]. Both Cu- and Fe-exchanged zeolites (most notably Cu- and Fe/ZSM-5) have been extensively studied as hydrocarbon and ammonia SCR catalysts [3–6]. SCR of NO_x with ammonia using metal-exchanged

small-pore molecular sieves with a Chabazite (CHA) structure, e.g. Cu/SSZ-13 and Cu/SAPO-34 [7,8], has been implemented a few years ago as part of the emission control systems for diesel passenger vehicles and heavy duty trucks in the U.S. and Europe. From 2010 till the present day, some 40 open literature publications have appeared, addressing various aspects of Cu/SSZ-13 and Cu/SAPO-34 NH₃-SCR catalysts [9,10]. It is somewhat surprising that Fe-exchanged CHA has received little attention during this period, considering the structural simplicity of CHA as compared with other commonly used zeolites (ZSM-5, beta, Y, etc.), and the benefits for this structural simplicity toward better understanding the nature of the active Fe species in NH₃-SCR. Note especially that after decades of extensive investigations, the nature of active Fe species in Fe/ZSM-5 is still not fully understood [6,11–14]. In the present study, for the first time we systematically investigate the synthesis and NH₃-SCR kinetics for Fe/SSZ-13 catalysts, and

Table 1
Si, Al and Fe contents, Si/Al and Fe/Al ratios, and BET surface areas and micropore volumes (from the t-plot method) of the fresh and HTA Fe/SSZ-13 samples.

Sample	Si content (%)	Al content (%)	Fe content (%)	Si/Al ratio	Fe/Al ratio	BET surface area (m^2/g)	Micropore volume (cm^3/g)
Fresh	40	3.2	1.37	12	0.2	547	0.282
HTA	Not analyzed (n.a.)	n.a.	n.a.	n.a.	n.a.	525	0.283

utilize two *ex situ* methods, i.e., Mössbauer spectroscopy and FTIR of adsorbed CO/NO to probe the nature of the catalytically active Fe species.

2. Experimental

2.1. Catalyst synthesis

A Na/SSZ-13 sample with Si/Al = 12 was hydrothermally synthesized using a method modified slightly from a protocol developed recently by Deka, et al. [15]. Composition of the gel was the following: 10SDA:10NaOH:4Al$_2$O$_3$:100SiO$_2$:2200H$_2$O. The gel was prepared by first dissolving NaOH (99.95%, Aldrich) in water and adding the SDA (TMAda-OH, Sachem ZeoGen 2825). Following which, Al(OH)$_3$ (containing ∼54% Al$_2$O$_3$, Aldrich) and fumed silica (0.007 μm average particle size, Aldrich) were added sequentially under vigorous stirring until the gel was homogenized. The gel (with a stir bar in) was then sealed into a 125 ml Teflon-lined stainless steel autoclave. Thereafter, the autoclave was placed in a salt bath on top of a hot plate stirrer to carry out hydrothermal synthesis at 160 °C for 96 h under stirring (300 rpm). After synthesis, Na/SSZ-13 was separated from the mother liquid via centrifugation and washed with deionized water for 3 times. Finally, the zeolite powders were dried at 120 °C under flowing N$_2$, and calcined in static air to remove the SDA. In this latter process, a thin layer of powder sample well-dispersed in a ceramic plate was heated to 550 °C at 2 °C/min and maintained at 550 °C for 8 h. Si and Al contents of the product powders were measured with Inductively Coupled Plasma Atomic Emission Spectroscopy (ICP-AES) at Galbraith Laboratories (Knoxville, TN, USA). Prior to measurements, the sample was dehydrated at 150 °C for 2 h in vacuum to remove adsorbed moisture.

Fe/SSZ-13 was prepared using a two-step solution ion exchange protocol. First, Na/SSZ-13 was exchanged to NH$_4$/SSZ-13 using 0.1 M NH$_4$NO$_3$ solution at 80 °C [16]. Second, 1 g of NH$_4$/SSZ-13 was dispersed in 100 ml of deionized water with pH adjusted to ∼3.0 using 0.1 M HNO$_3$. Thereafter, the suspension was heated to 80 °C with pure N$_2$ bubbling through to remove air dissolved in water and trapped in the zeolite pores. Next, still with the continuous protection of an N$_2$ atmosphere, FeSO$_4$·7H$_2$O powder (0.001 mole) was added into the suspension to carry out ion exchange at 80 °C for 1 h. Note that Cu^{2+} ions are readily exchanged into SSZ-13 at 80 °C via solution ion-exchange [16]. In principle, smaller sized Fe^{2+} ions should also be readily exchanged at the same temperature. However, it is important to prevent Fe^{2+} ions from being oxidized to bulky Fe^{3+} moieties (e.g., FeO(OH)) that are difficult to penetrate into zeolite pores [17]. In the present study, this was achieved by N$_2$ gas protection and maintaining a low pH during ion exchange. Fe/SSZ-13 was collected via centrifugation separation, washed multiple times with deionized water, dried at 120 °C in flowing N$_2$, and finally calcined in air at 550 °C for 5 h (denoted as fresh sample here). Some fresh sample was hydrothermally aged in the presence of 10% water vapor at 800 °C for 16 h (denoted as HTA sample).

2.2. Catalyst characterization

Fe, Si and Al contents for the fresh Fe/SSZ-13 sample were determined with ICP-AES. Based on the values obtained, the Fe/Al ratio was determined to be 0.2. Note also that dealumination does not occur during ion exchange at pH of ∼3.0 (i.e., the Si/Al ratio was maintained before and after ion exchange). BET surface areas and micropore volumes of the fresh and aged samples were measured with a Quantachrome Autosorb-6 analyzer. Prior to analysis, the samples were dehydrated under vacuum overnight at 250 °C. Table 1 summarizes Si, Al and Fe contents, Si/Al and Fe/Al ratios (for the fresh sample only), and BET surface areas and micropore volumes (from the t-plot method) of fresh and HTA samples. Powder X-ray diffraction (XRD) measurements were performed on a Philips PW3040/00 X'Pert powder X-ray diffractometer with Cu K$_\alpha$ radiation (λ = 1.5406 Å). Data were collected with 2θ ranging from 5° to 50° using a step size of 0.02°. ^{27}Al magic angle spinning nuclear magnetic resonance (MAS NMR) analysis of the fresh and HTA Fe/SSZ-13 samples was conducted on a Varian VNMRS system. Experimental details can be found elsewhere [18].

The *in situ* 'static' transmission IR experiments were conducted in a home-built cell housed in the sample compartment of a Bruker Vertex 80 spectrometer that has been described in detail previously [19]. In short, powder samples were pressed onto a tungsten mesh that can be resistively heated or cooled by liquid nitrogen. Unless otherwise specified, samples were annealed in vacuum (∼1 × 10^{-7} Torr) at 500 °C for 2 h and cooled back to ambient temperature prior to background spectra acquisition. Then, CO/NO was introduced in a pulse mode (∼0.02 Torr for the first pulse, until the total pressure reached ∼0.5 Torr). At each CO/NO pressure, a spectrum was taken after the pressure had equilibrated.

Sample preparation for Mössbauer spectroscopy measurements was identical to the procedure reported previously by Peretyazhko, et al. [20]. Briefly, ∼75–100 mg of hydrated ambient powder sample was initially mixed with Vaseline in a hollow Cu Mössbauer sample holder (0.95 cm by 1.27 cm) that was sealed at one end with Kapton tape. After thoroughly mixing Vaseline and sample, the other end of the holder was also sealed with Kapton tape. To ensure tightness, rings made of carbonized polyethyl-ether-ketone (PEEK) polymer were snapped onto the holder at both the ends. The spectra of the samples were collected using either a WissEl Elektronik (Germany) or Web Research Company (St. Paul, MN) instrument that included a closed-cycle cryostat SHI-850 obtained from Janis Research (Wilmington, MA), a Sumitomo CKW-21 He compressor unit (Wilmington, MA), and an Ar-Kr proportional counter detector with WissEl setup or a Ritverc (St. Petersburg, Russia) NaI detection system. A ^{57}Co/Rh source (50–75 mCi, initial strength) was used as the gamma energy source. With the WissEl setups, the transmitted counts were stored in a multichannel scalar (MCS) as a function of energy (transducer velocity) using a 1024-channel analyzer. The setups data were folded to 512 channels to provide a flat background and a zero-velocity position corresponding to the center shift (CS) of a metal Fe foil at room temperature (RT). Calibration spectra were obtained with a 25 μm thick Fe foil (Amersham, England) placed in the same position as the samples to minimize any geometry errors. The Mössbauer data were modeled with RecoilTM software (University of Ottawa, Canada) using a Voigt-based structural fitting routine.

NH$_3$ temperature programmed desorption (NH$_3$-TPD) was used to probe "residual" Brønsted acid sites in the samples. NH$_3$-TPD was carried out using our SCR reaction system with NH$_3$ detection via gas-phase FTIR. 60 mg catalysts (0.177–0.25 mm) were used for each measurement and the following experimental steps were followed: (1) Heat the sample to 550 °C in O$_2$/N$_2$ (300 sccm, 14% O$_2$)
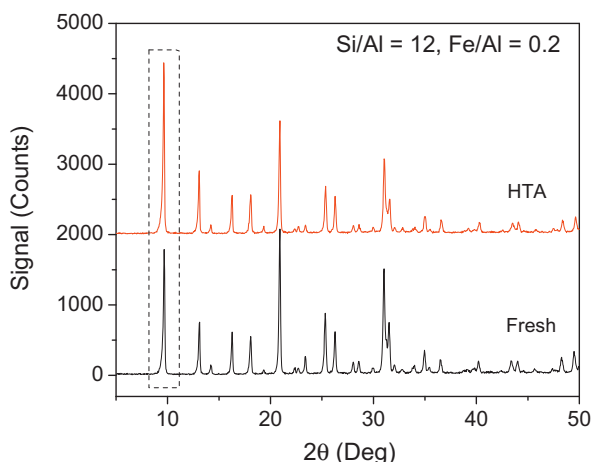
Fig. 1. XRD patterns for the fresh and hydrothermally aged (HTA) Fe/SSZ-13 samples.

and keep at $550\,^\circ$C for 30 min; (2) Stop O_2 flow, maintain N_2 flow, cool sample to $100\,^\circ$C; (3) Adsorb NH_3 ($\sim$500 ppm in N_2) until outlet NH_3 concentration stays constant for 1 h; (4) Turn off the NH_3 flow and purge with N_2 for 1 h; (5) Ramp from 100 to $600\,^\circ$C at $10\,^\circ$C/min, and maintain at $600\,^\circ$C until NH_3 desorption is complete.

2.3. NO/NH$_3$ oxidation and standard/fast NH$_3$-SCR reaction tests

NO/NH_3 oxidation and NH_3-SCR reaction kinetics were measured using a plug-flow reaction system described elsewhere [16]. Powder samples were pressed, crushed and sieved (0.177–0.25 mm) prior to use. For "standard" (i.e., $NO_x = NO$) SCR, the feed gas contained 350 ppm NO, 350 ppm NH_3, 14% O_2, and balance N_2. For "fast" (i.e., $NO_x = \frac{1}{2}\,NO + \frac{1}{2}\,NO_2$) SCR, the feed gas contained 175 ppm NO and 175 ppm NO_2, and other components were the same as standard SCR. NO (NH_3) oxidation reaction was conducted in the same manner, without adding NH_3 (NO) to the feed. Reactions were carried out under both 'dry' and 'wet' conditions. For 'wet' reactions, $\sim$2.5% H_2O was introduced to the feed by passing carrier N_2 through a bubble generator. For 'dry' reactions, this step was avoided. Most kinetic measurements were conducted at steady-state. Some non-steady-state measurements were also performed by linearly heating the samples from 100 to $500\,^\circ$C and cooling back to $100\,^\circ$C at $2\,^\circ$C/min. All of the gas lines were heated to over $100\,^\circ$C to avoid water condensation. The total gas flow was 300 sccm, and the gas hourly space velocity (GHSV) was estimated to be $\sim$200,000 h^{-1} for a catalyst amount of 60 mg. Concentrations of reactants and products were measured by an online Nicolet Magna 560 FTIR spectrometer with a 2 m gas cell maintained at $150\,^\circ$C. In this study, catalytic performance is mainly reported as conversion-temperature (i.e., light-off) curves. Equations used to calculate reactant conversions can be found elsewhere [16].

3. Results

3.1. Characterization results

Fig. 1 presents XRD patterns for the fresh and HTA Fe/SSZ-13 samples. Note that the quite harsh hydrothermal aging at $800\,^\circ$C for 16 h in the presence of 10% water vapor does not damage the CHA structure. This is fully consistent with BET surface and pore volume results displayed in Table 1, which also show minimal changes before and after aging. Meanwhile, no diffraction peaks assignable to iron oxides are found for either sample. Closer examination of
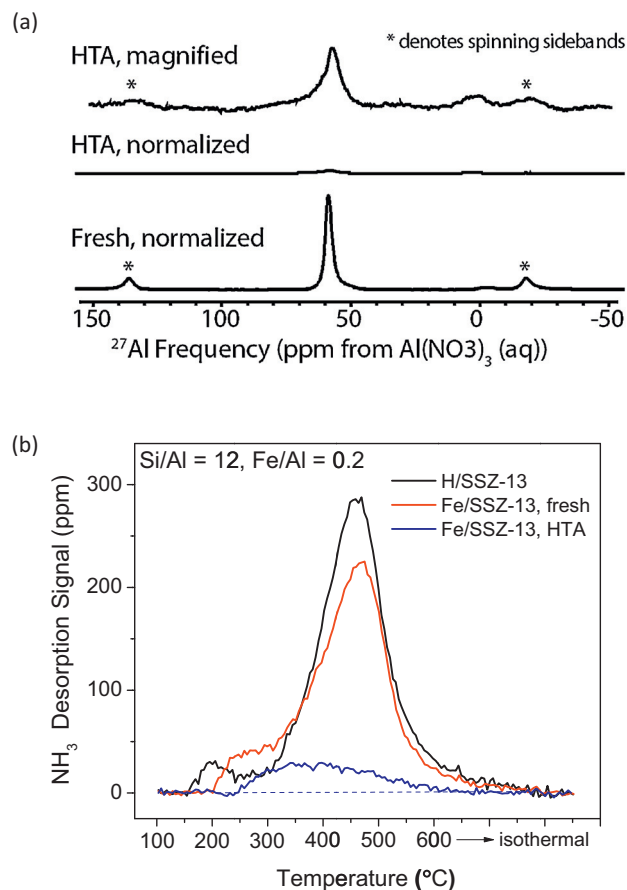

Fig. 2. (a) Solid state ^{27}Al-NMR spectra of the fresh and HTA Fe/SSZ-13 samples. (b) NH_3 temperature-programmed desorption (NH_3-TPD) curves for the parent H/SSZ-13, and the fresh and HTA Fe/SSZ-13 samples. NH_3 adsorption and purging are carried out at $100\,^\circ$C. Samples are ramped from 100 to $600\,^\circ$C at $10\,^\circ$C/min and maintained at $600\,^\circ$C for 30 min. NH_3 desorption is monitored with an on-line FTIR detector.

the XRD patterns does reveal that the relative signal intensity of the diffraction peak at 9.6° (diffraction from the (1 0 0) plane, highlighted with a dashed rectangle) is enhanced after HTA. This may indicate that Fe ions move away from the less rigid 8-membered rings (8MR) during HTA. This follows since metal ions close to 8MR tend to deform them thus lowering reflection from the (1 0 0) plane.

Fig. 2(a) presents ^{27}Al MAS NMR results of the fresh and HTA Fe/SSZ-13 samples. The bottom spectrum is for the fresh sample and the middle spectrum is for the HTA sample. The two spectra are mass and scan number normalized for direct comparison. The upper spectrum shows a magnified spectrum for the HTA sample for more details. The spectrum for the H/SSZ-13 sample resembles that of the fresh Fe/SSZ-13 and is not given. Two points are worth addressing here: (1) In the fresh sample, framework Al (Al$_f$, at $\sim$60 ppm) dominates while the extra-framework Al (at $\sim$0 ppm) content is negligible. (2) Upon hydrothermal aging, Al$_f$ content greatly diminishes suggesting extensive dealumination. However, the signal for extra-framework octahedral Al (expected to form as a result of dealumination) at $\sim$0 ppm does not increase. This indicates strong interactions between paramagnetic Fe species and octahedral Al in the HTA sample rendering it "invisible". The same phenomenon has been observed previously on our hydrothermally aged Cu/zeolites for the same reason [21]. Note also that it is not uncommon that zeolite dealuminate under high-temperature hydrothermal conditions without exhibiting significant damage to their crystal structures [21]. From Fig. 1, this is apparently the case for the HTA Fe/SSZ-13 sample here.

Fig. 2(b) depicts NH_3 temperature-programmed desorption (NH_3-TPD) curves for H/SSZ-13 and Fe/SSZ-13 samples (fresh and HTA). For the H/SSZ-13 sample, a very weak desorption state is found at ~200 °C. This is due to NH_3 desorption from weak acid sites (e.g., extra-framework Al). The majority of NH_3 desorbs at much higher temperatures (centered at ~480 °C), due to desorption from Brønsted acid sites. For the fresh Fe/SSZ-13 sample, the TPD curve is rather asymmetric and includes perhaps two shoulder features below ~400 °C. Although not very well-resolved, these are likely due to NH_3 desorption from weak acidic and iron cation sites. Interestingly, the intensity of the NH_3 desorption signal from Brønsted acid sites decreased ~20% as compared to the parent H/SSZ-13. As noted above, an Fe/Al ratio of 0.2 was obtained for our Fe/SSZ-13 sample from ICP-AES analysis. From Fig. 2(a), the amount of extra-framework Al is negligible indicating H^+/Al ratio of ~1 in the parent H/SSZ-13. It can be estimated, therefore, that during solution ion exchange, each Brønsted acid site is exchanged with one Fe ion (i.e., $H^+/Fe^{2+} = 1$). Note that such a 1/1 exchange ratio has been found previously for Fe/ZSM-5 formed from solution ion exchange [22]. With the aid from Mössbauer spectroscopic data, this will be discussed in more detail below. Also from Fig. 2(b), the amount of NH_3 desorption from the HTA sample was significantly lower than that from the fresh sample consistent with the ^{27}Al NMR results shown in Fig. 2(a). Note, however, that both XRD and surface area/pore volume measurements reveal little structural damage during the HTA treatment.

Variable temperature ^{57}Fe-Mössbauer spectroscopy was used to investigate the nature of Fe species in the fresh and HTA Fe/SSZ-13 samples. Hydrated samples (i.e., samples stored in ambient conditions and saturated with moisture) were used for the measurements. Fig. 3(a) and (b) displays spectra acquired at room temperature (RT) and 77 K (LN), respectively, for the fresh sample, and Fig. 4(a) and (b) presents RT and LN spectra for the aged sample. Key parameters obtained after fitting the experimental doublet data, i.e., Center Shift (CS, mm/s), Quadrupole Splitting (QS, mm/s), Quadrupole Shift (ε, mm/s), Hyperfine Magnetic Field (HF, Tesla), and phase quantification results are listed in Table 2. For the fresh sample at RT, best fitting gives primarily two iron components. These two moieties are denoted as Fe(III)-RT-1 (sharp doublet; CS = 0.36 mm/s; QS = 0.84 mm/s) and Fe(III)-RT-2 (broad doublet; CS = 0.5 mm/s; QS = 1.68 mm/s), respectively. These parameters demonstrate that: (1) both iron components are Fe(III) moieties; and (2) their coordination numbers are higher than tetrahedral coordination [23–25]. Fe(III)-RT-1 has a QS = 0.84 mm/s suggesting that a diferric μ-hydroxo complex or a high-spin monoferric complex can be assigned to this signal [24]. In light of the fact that our sample was fully hydrated and diferric species can hydrolyze to monoferric species [23], this is tentatively assigned to a monoferric species (i.e., $[Fe(OH)_2]^+$). The high QS = 1.86 mm/s of Fe(III)-RT-2 strongly suggests that it is a diferric μ-oxo complex (i.e., $[HO—Fe—O—Fe—OH]^{2+}$) [25].

In order to make more precise identification of Fe-speciation in this sample, a spectrum was also obtained at 77 K. This approach was essential to distinguish Fe species of different magnetic states that are difficult to model at RT due to overlapping parameters, and to identify Mössbauer silent Fe-species at RT. For example, the spectral features of the fresh sample at 77 K (Fig. 3(b)) are dominated by 4 components: (a) an Fe(II) doublet that was non-existent at RT (Fe(II)-LN-1, CS = 1.62 mm/s and QS = 2.87 mm/s); the CS and QS values of Fe(II)-LN-1 are within the range of ferrous species [23–26]. The detection of Fe(II) only below RT suggests that at RT it exists as a highly-mobile ferrous species, or undergoes significant recoil on γ-ray absorption since only recoil-free absorption results in Mössbauer signal. Note that Fe(II) in hydrated Y,FAU zeolite is also invisible at RT but becomes detectable at lower temperatures [26]. (b) An intense Fe(III) doublet assignable to hydrated
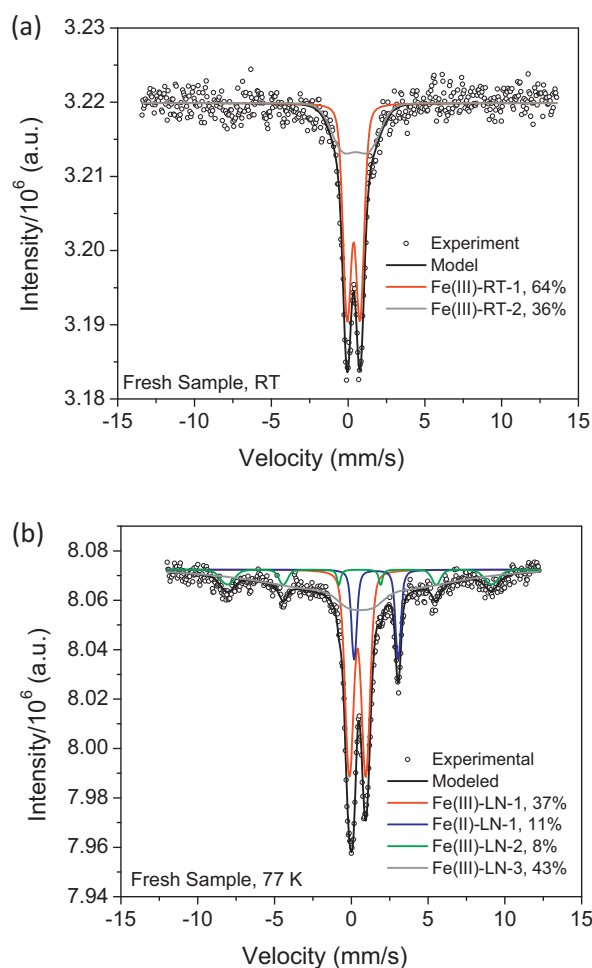
monoferric species (Fe(III)-LN-1; CS = 0.41 mm/s; QS = 1.07 mm/s), that was a significant fraction of the Fe(III)-RT-1 doublet. (c) A minor FeO_x cluster sextet (Fe(III)-LN-2; CS = 0.41 mm/s; ε = −0.01 mm/s) due to magnetic ordering (or transformation of RT doublet to sextet at 77 K) of a small fraction of the Fe(III)-RT-1. (d) Finally, a broad Fe(III) feature is due to diferric μ-oxo complex that existed as Fe(III)-RT-2 doublet at RT (Fe(III)-LN-3; CS = 0.3 mm/s; ε = −0.3 mm/s).

The RT Mössbauer spectrum of the HTA Fe/ZZS-13 sample is dominated by an asymmetric doublet, implying contributions from more than one species. Nevertheless, as shown in Fig. 4(a) and Table 2, its modeled CS = 0.33 and QS = 1.35 mm/s parameters demonstrate that all detectable iron species at RT are in a +3 oxidation state. The feature is denoted as Fe(III)-RT-3. At 77 K, three components are obtained: (a) an Fe(III)-LN-4 doublet (CS = 0.44 mm/s; QS = 1.22 m/s; dominant species); (b) Fe(III)-LN-5 sextet (CS = 0.54 mm/s; ε = −0.24 mm/s; HF 51.7 Tesla); and (c) Fe(II)-LN-2 doublet (CS = 1.56 mm/s; QS = 2.76 mm/s). Note that this latter ferrous species was not evident at RT, as also the case for the fresh sample. Clearly, the majority of Fe(III)-RT-3 transforms to Fe(III)-LN-4 in this case with some minor transformation to the well-defined sextet, Fe(III)-LN-5. The parameters of the Fe(III)-LN-5 are little lower than the Mössbauer spectral parameters of Fe(III)-LN-2 in the fresh sample, particularly HF magnitude (51.7 Tesla vs. 53.34 Tesla, Table 2), which may be due to some Al inclusion in the FeO_x clusters [27]. It is important to note that its content, however, is similar to FeO_x of the fresh sample. Finally, Fe(III)-LN-2 evident
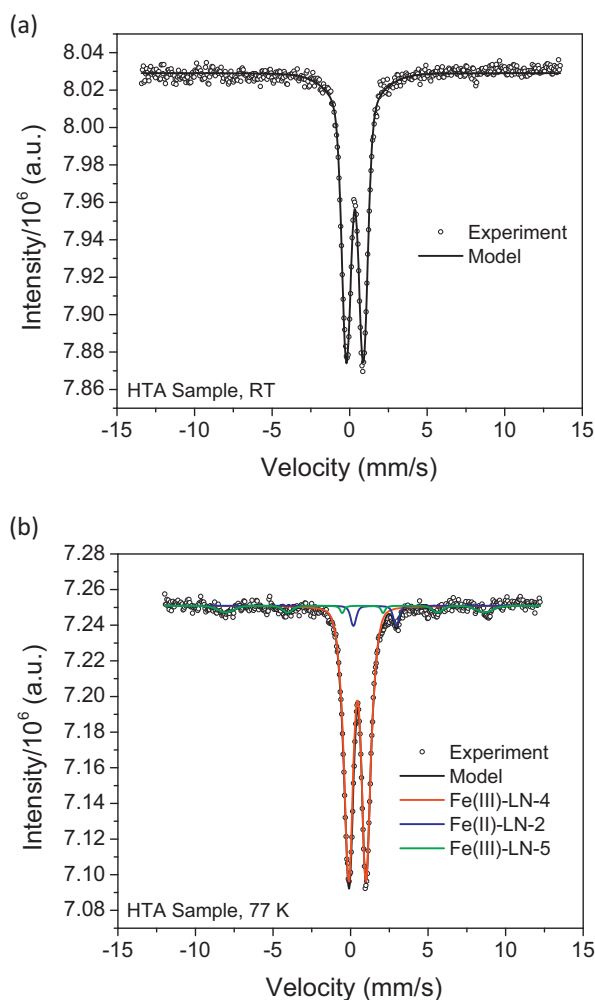

Fig. 3. Mössbauer spectra of the hydrated fresh Fe/SSZ-13 sample at room temperature (a), and at 77 K (b).

Fig. 4. Mössbauer spectra of the hydrated HTA Fe/SSZ-13 sample at room temperature (a), and at 77 K (b).

Fig. 5. Series of selected IR spectra obtained after exposure of annealed fresh (a) and HTA (b) Fe/SSZ-13 samples to CO at 150 K. The samples were annealed in vacuum at 773 K for 2 h prior to IR measurements.

in the fresh sample is absent in the HTA sample. This implies that this phase is unstable and has transformed to Fe(III)-LN-4 doublet upon ageing.

CO/NO titration FTIR experiments were conducted to further probe the fresh and HTA Fe/SSZ-13 samples. Prior to the measurements, the samples are first outgassed in high vacuum ($\sim 10^{-7}$ Torr) at 500 °C for 2 h. Note that at least some of the Fe(III) moieties are reduced to Fe(II) during this process by auto-reduction. Therefore, the nature of Fe species in the IR experiments is almost certainly different from that under highly oxidizing and humid SCR reaction conditions. Yet, CO/NO titration FTIR is still very informative,
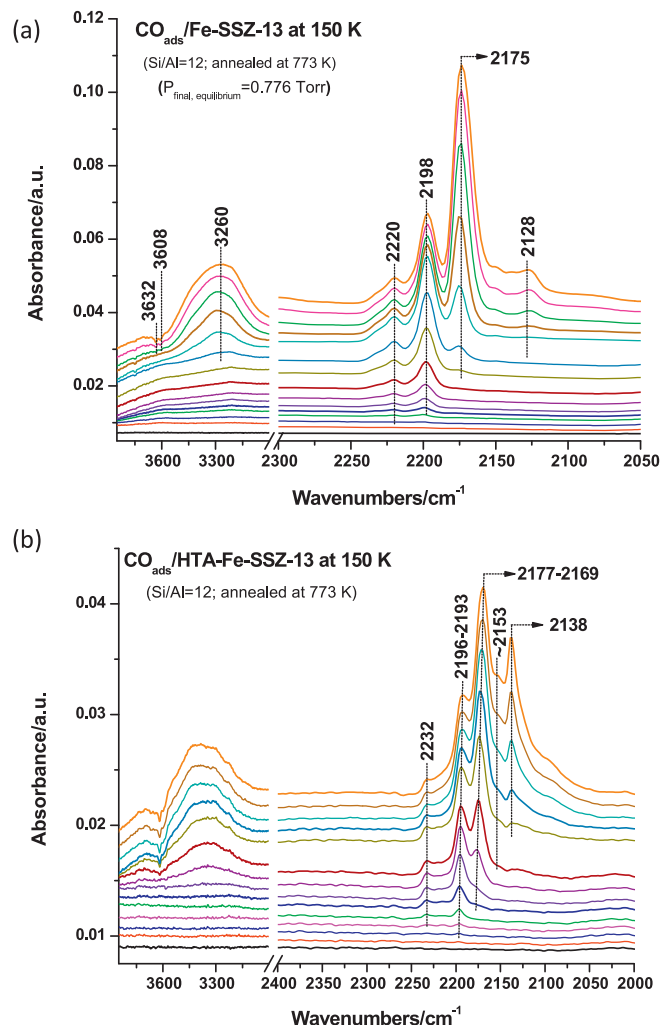
especially in determining whether metal ions are in charge-balancing sites and, if so, which ones.

Fig. 5(a) presents CO adsorption spectra at 150 K for the fresh sample. 4 bands are observed in the CO stretching vibrational (ν_{CO}) regime. At the lowest CO pressure, a band at 2198 cm^{-1} develops first. With increasing CO pressure, bands at 2220, 2175 and 2128 cm^{-1} develop sequentially. Based on previous studies, the 2198 cm^{-1} band is attributed to Fe^{2+}—CO, and the 2220, 2175 and 2128 cm^{-1} features are assigned to Al^{3+}—CO, an OH—CO adduct, and an OH—^{13}CO adduct from natural ^{13}C abundance in CO, respectively

Table 2
Simulated key Mössbauer parameters and estimated percentages of various Fe components in the fresh and HTA Fe/SSZ-13 samples measured at room temperature and 77 K.

Sample	Measurement condition	Component	Center shift, (CS, mm/s)	Quadrupole splitting, (QS, mm/s)	Quadrupole shift, (ε, mm/s)	Hyperfine magnetic field, (HF, Tesla)	Percentage (%)
Fresh	RT	Fe(III)-RT-1	0.36	0.84	–	–	64
		Fe(III)-RT-2	0.5	1.86	–	–	36
	77 K	Fe(III)-LN-1	0.41	1.07	–	–	37
		Fe(III)-LN-2	0.54	–	-0.01	53.34	8
		Fe(III)-LN-3	0.3	–	-0.3	29	43
		Fe(II)-LN-1	1.62	2.87	–	–	11
HTA	RT	Fe(III)-RT-3	0.33	1.35	–	–	100
	77 K	Fe(III)-LN-4	0.44	1.22	–	–	89
		Fe(III)-LN-5	0.54	–	-0.24	51.7	7
		Fe(II)-LN-2	1.56	2.76	–	–	4

[28,29]. In the OH vibrational regime, weak negative features are found at 3632 and 3608 cm^{-1}. These are due to CO perturbation of the —OH groups (Fe^{n+}—OH and Al^{3+}—OH, respectively), consistent with OH—CO adduct formation observed in the ν_{CO} regime. Concomitantly a broad feature centered at 3260 cm^{-1} also gradually develops, as a consequence of the redshift in the ν_{O-H} vibrations as the OH groups interact with CO (perturbed ν_{O-H} vibrations). The corresponding spectra for the HTA sample are displayed in Fig. 5(b). With increasing CO pressure, the bands observed on the fresh sample are also found, and their development follows the same sequence. Notably, new bands at 2138 and 2153 cm^{-1} (as a shoulder) are observed on the HTA sample. The nature of these bands is not exactly clear, but Fe^{2+}—CO species perturbed by metal cations in close proximity are possible, and more discussion regarding these features will be given below.

Fig. 6(a) presents NO adsorption FTIR spectra for the fresh sample at 295 K. At the lowest NO pressure, a ν_{NO} band develops at 1885 cm^{-1} which can be assigned to Fe^{2+}—NO [30–36]. At slightly higher NO pressures, two ν_{NO} bands develop simultaneously at 1771 and ~1850 cm^{-1}, where the latter appears as a shoulder feature of the stronger 1885 cm^{-1} band. These bands can be assigned to dinitrosyl, i.e., Fe^{2+}(NO)$_2$ species [32,34–36]. Meanwhile, weak IR features also appear at 2158 cm^{-1} (assigned to NO$^+$) and below 1700 cm^{-1} (adsorbed NO$_2$ and nitrate species) [19,37]. As the NO pressure continues to rise, intensities of all these bands increase, while new ν_{NO} features at 1915/1812/1800 cm^{-1} grow simultaneously. These latter features are assigned to trinitrosyl, i.e., Fe^{2+}(NO)$_3$ species [32,34–36]. A weak feature at 2250 cm^{-1}, due to adsorbed N$_2$O, also develops at the highest NO pressures [19,37]. Following the NO adsorption experiment, the system was evacuated to ~1 × 10^{-7} Torr and the sample was annealed stepwise from 295 to 500 K. Spectra were acquired to test the thermal stabilities of the various IR bands and the results are plotted in Fig. 6(b). Immediately upon evacuation at 295 K, the 1915/1812/1800 cm^{-1} bands (Fe^{2+}(NO)$_3$) disappear, as does the adsorbed N$_2$O peak. With increasing temperature, the 1850/1771 cm^{-1} bands (Fe^{2+}(NO)$_2$) disappear next, followed by the Fe^{2+}—NO species that gives rise to the 1885 cm^{-1} band. However, the NO$^+$ species at 2158 cm^{-1} and the NO$_2$/nitrate species below 1700 cm^{-1} are stable up to 500 K. It is also interesting to note that new bands at 1898 and 1795 cm^{-1} appear during annealing. Their nature will be addressed in a separate publication. Despite the debates in the literature on the precise assignments of these nitrosyl moieties [30,34,36], there is a high degree of confidence that the majority of Fe species in our fresh sample are in extra-framework cationic positions. This follows since all of the NO vibrational bands observed in the present study have counterparts on other Fe/Zeolites in which Fe is known to be in cationic positions [30–36]. Note that the Mössbauer spectra for the fresh sample (Fig. 3) lead to the same conclusion in spite of the fact that Mössbauer probes all Fe species while CO/NO titration FTIR only probes Fe^{2+} species.

The RT NO adsorption FTIR spectra collected for the HTA sample are plotted in Fig. 6(c). At a first glance, the spectra look very different from the fresh sample and the overall signal intensity is substantially lower. These indicate that both the nature and the availability of iron sites undergo considerable changes during HTA. At the lowest NO pressures, a ν_{NO} band first develops at 1875 cm^{-1}. As the NO pressures rise, this feature appears to maintain its frequency and eventually becomes a shoulder peak of a group of broad and overlapping bands in the range from ~1950 to ~1750 cm^{-1}. The strongest among these overlapping bands is found at ~1870 cm^{-1}, which gradually red-shifts to ~1850 cm^{-1} as the NO pressure increases. A weak, but clearly distinguishable feature is also found at 1772 cm^{-1}. There appear to also be bands at 1915, 1897 and 1815 cm^{-1}; however, these are much less well-resolved. Note finally that at higher frequencies, the 2248 cm^{-1} N$_2$O
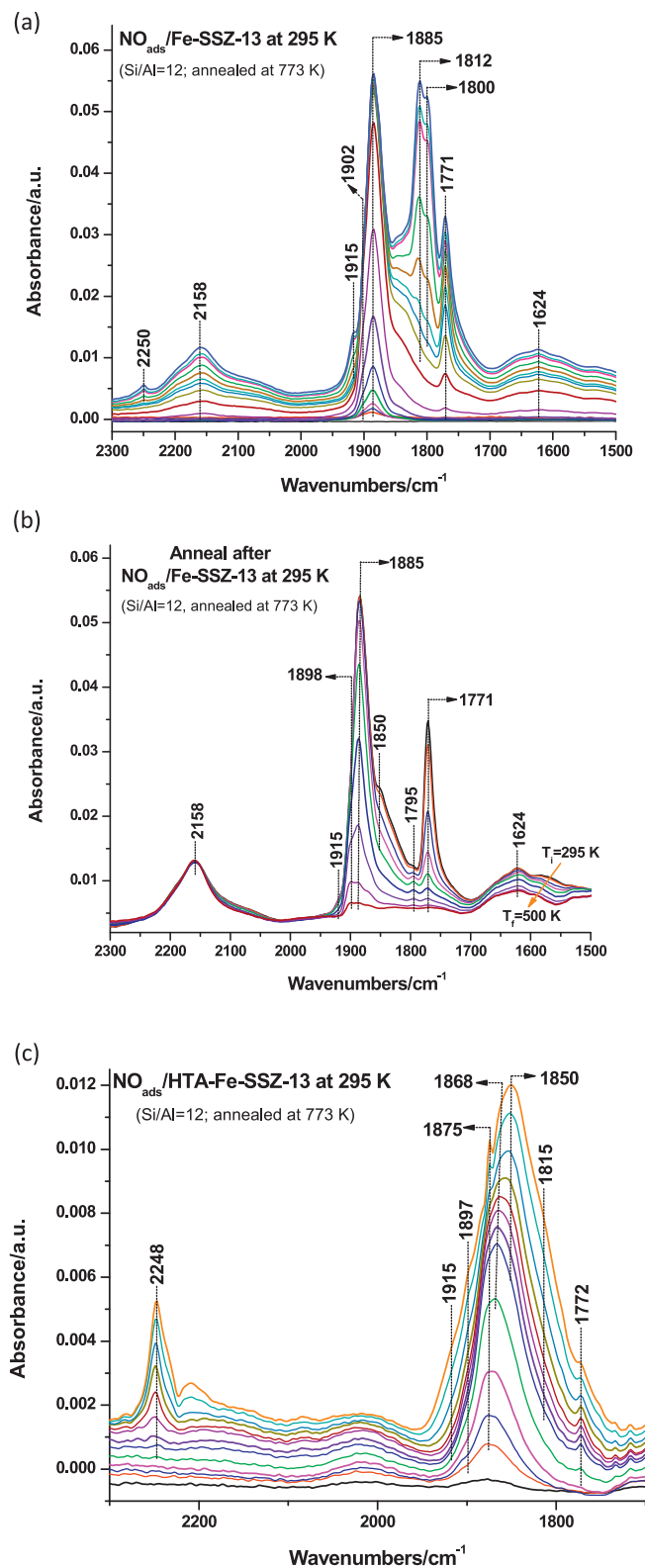

Fig. 6. (a) Series of selected IR spectra obtained after exposure of annealed fresh Fe/SSZ-13 sample to NO at 295 K. (b) Spectra obtained after evacuating the IR cell and annealing the sample from 295 to 500 K following the NO adsorption step for the fresh Fe/SSZ-13 sample. (c) Series of selected IR spectra obtained after exposure of annealed HTA Fe/SSZ-13 sample to NO at 295 K. The samples were annealed in vacuum at 773 K for 2 h prior to IR measurements.
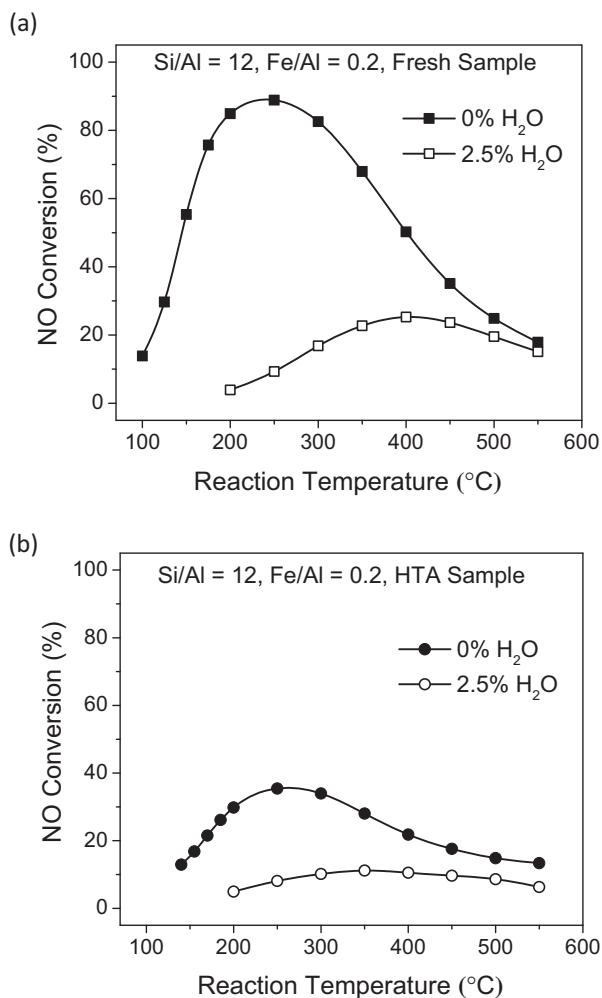
Fig. 7. NO conversions as a function of temperature during NO oxidation for the fresh (a) and HTA (b) Fe/SSZ-13 samples. Reactant feed contains 350 ppm NO, 14% O_2, none or 2.5% H_2O balanced with N_2 at a GHSV of 200,000 h^{-1}.

Fig. 8. NH_3 conversions as a function of temperature during NH_3 oxidation for the fresh (a) and HTA (b) Fe/SSZ-13 samples. Reactant feed contains 350 ppm NH_3, 14% O_2, none or 2.5% H_2O balanced with N_2 at a GHSV of 200,000 h^{-1}.

band is still observed on the HTA sample while the 2150 cm^{-1} band for NO$^+$ is no longer detected.

3.2. Reaction results

3.2.1. Steady-state reactions

Fig. 7 presents steady-state NO oxidation ($NO + ½ O_2 = NO_2$) reaction results under both 'dry' and 'wet' conditions where, for the latter, 2.5% H_2O was added to the reactant feed. As shown in Fig. 7(a), the fresh sample is very active for NO oxidation without the presence of H_2O, where NO conversions reach ~90% at 250 °C. At higher temperatures, NO conversions are limited thermodynamically [38]. In contrast, the reaction is severely inhibited by H_2O. In this case, a maximum NO conversion of ~23% is found at 400 °C. At even higher temperatures, the influence from thermodynamic limitations is still evident. As the results of Fig. 7(b) clearly show, the HTA sample is much less active than the fresh sample under both 'dry' and 'wet' conditions. Meanwhile, the H_2O inhibition effect is again evident. It is interesting to note that the lineshapes for the NO conversion-temperature curves for the fresh and HTA samples under 'dry' conditions are almost identical. This could mean that NO oxidation is carried out on similar sites in both samples whereas, for the HTA sample, the availability of and/or access to such sites is much less. Note also that for both samples, NO_2 selectivity is always close to 100% at all reaction temperatures studied under
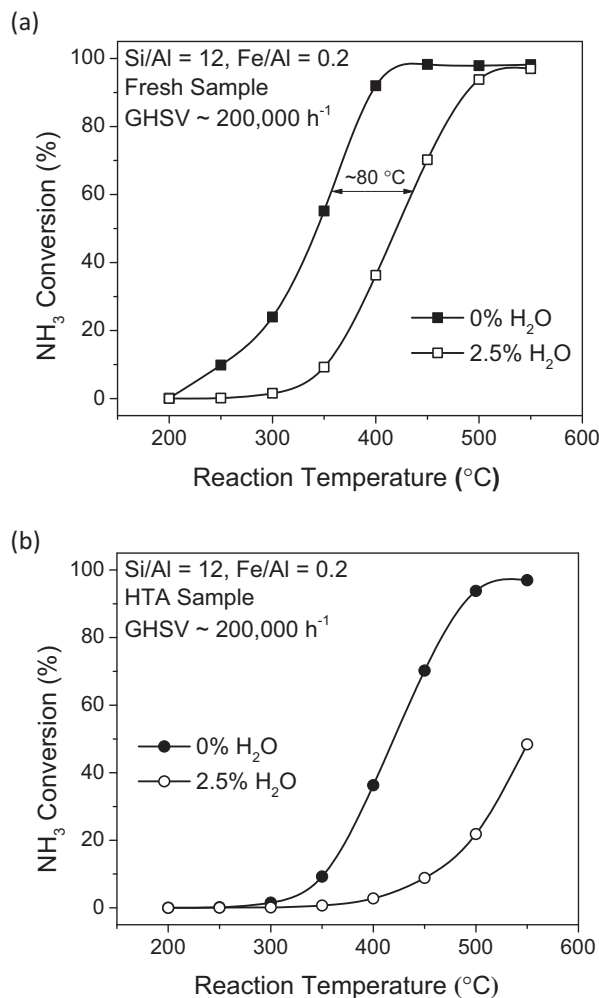
'wet' conditions. However, ~10% of NO undergoes decomposition ($2NO = N_2 + O_2$) instead of oxidation to NO_2 at temperatures higher than ~400 °C under 'dry' conditions (data not shown). Since this latter reaction channel is rather minor, it will not be further discussed here.

Fig. 8 presents steady-state NH_3 oxidation ($4NH_3 + 3O_2 = 2N_2 + 6H_2O$) reaction results under both 'dry' and 'wet' conditions. It is interesting to note from Fig. 8(a) that for the fresh sample, the lineshapes for the light-off curves under 'dry' and 'wet' conditions are almost identical except that, in the presence of H_2O, it shifts to higher temperatures by ~80 °C. This may suggest that H_2O and NH_3 compete for the same sites that catalyze NH_3 oxidation. As shown in Fig. 8(b), the HTA sample is much less active and the H_2O inhibition effect appears to be even more severe than in the fresh sample.

Steady-state standard NH_3-SCR reaction ($4NO + 4NH_3 + O_2 = 4N_2 + 6H_2O$) results on the fresh sample are plotted in Fig. 9(a), again with and without the presence of H_2O in the feed. A number of points are worth addressing here: (1) under 'wet' conditions, reaction starts above 200 °C and 50% NO/NH_3 conversion (T_{50}) occurs at ~290 °C. Under 'dry' conditions, similar to the NO/NH_3 oxidation reactions, an increase in low-temperature activity is also found where T_{50} decreases to ~260 °C. (2) Above ~250 °C, NH_3 conversions become 5–10% higher than NO conversions at the same temperature under 'wet' conditions due to the occurrence of
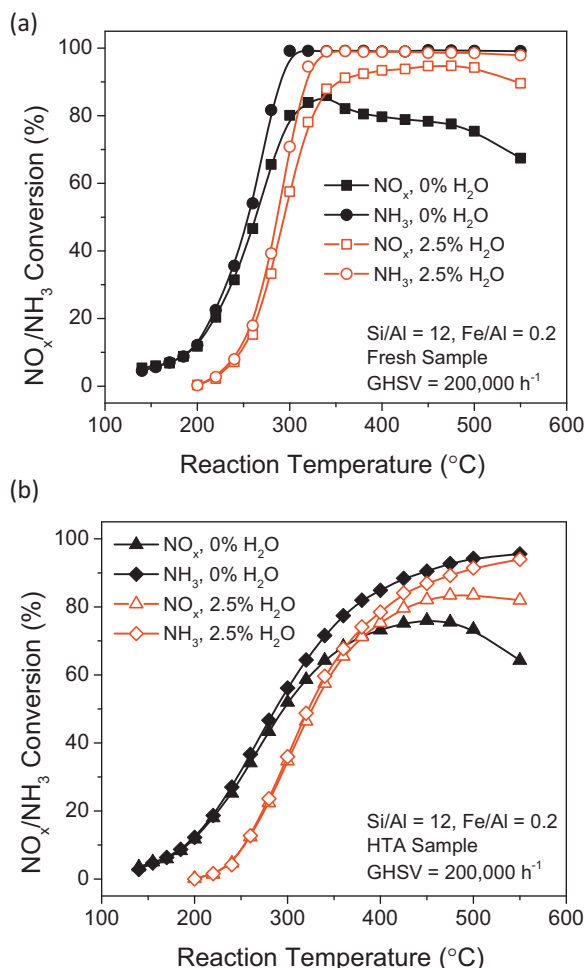
(a)

(b)

Fig. 9. NO_x/NH_3 conversions as a function of temperature during standard $NH_3 - SCR$ for the fresh (a) and HTA (b) Fe/SSZ-13 samples. Reactant feed contains 350 ppm NO, 350 ppm NH_3, 14% O_2, none or 2.5% H_2O balanced with N_2 at a GHSV of 200,000 h^{-1}.

non-selective NH_3 oxidation that competes with SCR [16]. Still, high and stable SCR selectivities of ∼90% are maintained in a wide temperature range from ∼350 to 550 °C. *(3)* Under 'dry' conditions, SCR becomes substantially less selective above ∼300 °C demonstrating more extensive non-selective NH_3 oxidation. This is fully in line with the NH_3 oxidation results shown in Fig. 8(a).

Fig. 9(b) depicts steady-state standard SCR results for the HTA sample. Under both 'wet' and 'dry' conditions, expectedly, this sample is less active than the fresh sample. By comparing NO and NH_3 conversion differences at identical reaction conditions for the fresh and HTA samples, it is found that SCR selectivities are generally higher for the HTA sample. Notably in the presence of moisture, SCR selectivities are above 90% even at 500 °C for this sample. We note that this is considerably different for Cu/SSZ-13 catalysts which typically show substantial SCR selectivity loss above ∼400 °C after severe hydrothermal aging [39,21].

3.2.2. Temperature-programmed reactions

In these experiments, after the reactant feed is turned on, the samples are first maintained at 100 °C for 1 h, then ramped to 500 °C at 2 °C/min, cooled back to 100 °C at 2 °C/min, and maintained at 100 °C for 1 h before the feed is turned off. Finally, after purging with dry N_2 at 100 °C for 1 h, a temperature-programmed desorption (TPD) experiment is conducted at 10 °C/min to desorb species that are adsorbed/deposited on the catalysts during reaction. Both standard- and fast-SCR are probed in this case. Note that
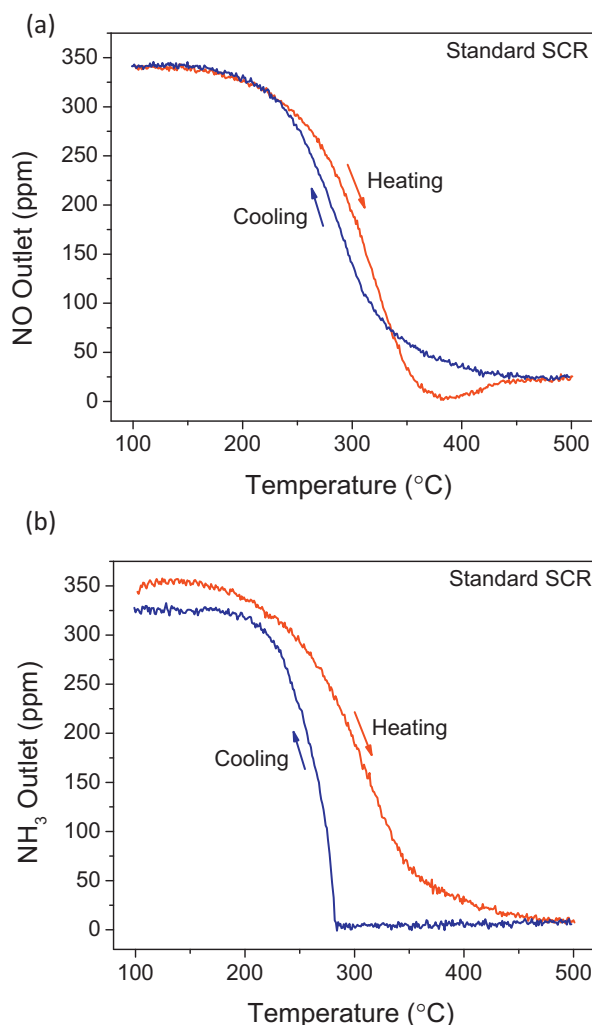
(a)

(b)

Fig. 10. NO (a) and NH_3 (b) outlets during temperature-programmed standard $NH_3 - SCR$ reaction on the fresh Fe/SSZ-13 sample. Reactant feed contains 350 ppm NO, 350 ppm NH_3, 14% O_2, 2.5% H_2O balanced with N_2 at a GHSV of 200,000 h^{-1}. The sample is exposed to the feed at 100 °C for 1 h and ramped to 500 °C at 2 °C/min, and then ramped from 500 to 100 °C at 2 °C/min, and maintained at 100 °C for 1 h before finish.

these measurements are a very good supplement to steady-state measurements in studying transient kinetic behaviors, kinetic hysteresis, NH_3 and NH_4NO_3 inhibitions, etc.

Fig. 10(a) presents NO outlet concentrations (in ppm, measured with an online FTIR cell) during temperature ramping for standard SCR. Note that the NO outlet during the isothermal step at 100 °C is not included in this plot. In two temperature ranges (i.e., 100–250 °C and 450–500 °C), no hysteresis is observed. However, from 250 to ∼330 °C, NO outlet values during heating are higher than that during cooling, while from 330 to 450 °C, NO outlet concentrations during heating are lower than that during cooling. Fig. 10(b) shows the corresponding NH_3 outlet values. During heating, NH_3 outlet concentrations gradually decrease and only become undetectable above 450 °C. However, during the cooling step, zero NH_3 outlet values are maintained until ∼290 °C and then increase abruptly as the temperature further decreases. Fig. 11 displays TPD results following the just-described temperature-programmed reaction steps. No NO_x (NO, NO_2 and N_2O) desorption is detected suggesting no NO_x or nitrate/nitrite species are deposited during reaction. The only species that are detected are NH_3 and H_2O. NH_3 starts to desorb at ∼250 °C with a desorption peak maximum found at ∼480 °C. Unambiguously, this
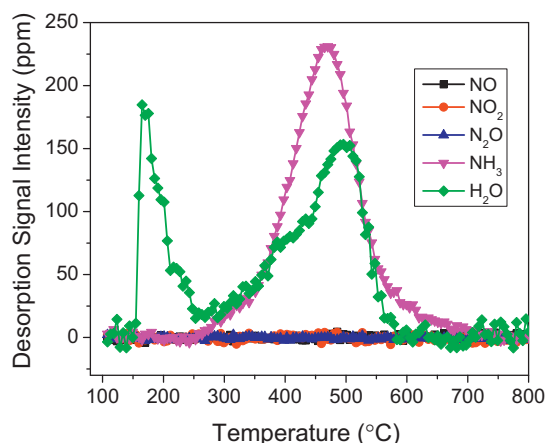
Fig. 11. Temperature-programmed desorption (TPD) of species adsorbed on the fresh Fe/SSZ-13 sample after the temperature-programmed standard SCR reaction step described in Fig. 10. Prior to TPD, the sample is purged with N_2 for 1 h at 100 °C, and then ramped from 100 to 800 °C at 10 °C/min.

is due to desorption of NH_3 adsorbed on Brønsted acid sites (e.g., see Fig. 2). H_2O has two desorption states: below ~250 °C, the peak is likely due to H_2O weakly held by the zeolite framework, for example, by hydrogen bonding. Desorption above ~250 °C (containing at least 3 sub-states) is assigned to dehydration of Fe-containing sites. This will be discussed in more detail below.

The same experiments were conducted under fast SCR conditions ($NO + NO_2 + 2NH_3 = N_2 + 3H_2O$). Fig. 12(a) presents NO_x outlet concentrations (including NO, NO_2, N_2O and the total NO_x) during heating/cooling. For NO, very minor hysteresis is found between ~200 and ~280 °C where outlet NO concentrations are slightly higher during heating indicative of some inhibition by NH_3 and/or NH_4NO_3. At temperatures above ~280 °C, no NO in the outlet is observed. The behavior of NO_2, however, is very different. In this case, the 1 h waiting period at 100 °C prior to temperature ramping is far from sufficient for the NO_2 outlet to reach the inlet concentration (175 ppm). This indicates extensive NO_2 storage. However, control experiments without co-feeding NH_3 demonstrate that the catalyst is only capable of storing much lower amounts of NO_2 (data now shown). Therefore, NO_2 must be storing as ammonium nitrate/nitrite in the presence of NH_3. This point is partially confirmed from the detection of N_2O between 200 and 300 °C during ramping up the catalyst. As has been well-documented, in this temperature range N_2O originates from NH_4NO_3 decomposition [40]. Since NO_x storage is not expected at temperatures where NH_4NO_3 becomes unstable, the lack of NO_x in the outlet above ~300 °C suggests that NO and NO_2 are completely converted to N_2. This result is fully expected since in the absence of NH_3/NH_4NO_3 inhibition (which is met at temperatures above ~300 °C), fast SCR can be expected to proceed more rapidly than standard SCR for Fe-based catalysts. During the cooling step, a notable point for NO_2 outlet values is that a concentration minimum is found at ~240 °C. The origin of this phenomenon is not clear. Fig. 12(b) plots the corresponding NH_3 outlet concentrations during the experiment. To some extent, these curves resemble the NO_x outlet curves shown in Fig. 12(a) but with some distinct differences. During the heating step, NH_3 outlet values do not decrease to zero above ~300 °C as do NO_x concentrations, due to desorption of stored NH_3 at lower temperatures. During the cooling step, NH_3 outlet values remain negligible until ~220 °C, much lower than ~300 °C at which NO_x concentrations start to be detected in the outlet. Again, this is due to the extra NH_3 storage at Brønsted acid sites.

Finally Fig. 13 presents the TPD results obtained after the temperature-programmed fast SCR reaction steps. Markedly

different from Fig. 11, in this case rather complicated NO_x desorption states are observed in the temperature range of ~200–330 °C suggesting more than one ammonium nitrate/nitrite decomposition pathway. A small, single NO desorption state is found at ~260 °C. NO_2 also appears to have a single desorption state at ~276 °C. N_2O displays two desorption states at ~250 (as a shoulder feature) and ~300 °C. NH_3 develops three desorption states at ~250, ~330 and ~470 °C, respectively. The ~250 °C peak can be assigned to NH_3 released via ammonia nitrate/nitrite decomposition. The ~330 °C state may be due to NH_3 desorption from Fe active centers, while the ~470 °C state is, again, due to NH_3 desorption from Brønsted acid sites. Finally the H_2O desorption state at ~300 °C is due to ammonium nitrate/nitrite decomposition while the higher temperature state at ~500 °C is due to dehydration of Fe active centers. The low-temperature H_2O desorption state seen after standard SCR (Fig. 11), is not seen in this case due presumably to NH_4NO_3 deposition during fast SCR.

4. Discussion

At the outset of this discussion section, we note that only one Fe/SSZ-13 catalyst (Si/Al = 12, Fe/Al = 0.2) has been used in the present study in order to maintain structural simplicity of the paper. Some important issues such as Si/Al ratio and Fe loading effects are not probed here but are currently under investigation. Since SCR over zeolite catalysts is a highly application-oriented research area, focus has been given to both fresh and severely hydrothermally aged samples. We note also that the catalyst characterization methods used in this study are *ex situ*; therefore, unambiguous structure-function relationships cannot be constructed at this time. Rather, our focus in this first report of Fe/SSZ-13 SCR catalysts is to introduce a number of interesting characteristics of this catalyst system, and to also point out some particularly interesting contrasts with the behavior of Cu/CHA materials. In doing so, we hope to highlight relevant and useful areas where follow-on studies might be especially fruitful. A detailed comparative study between Cu- and Fe/SSZ-13 SCR catalysts will be published elsewhere.

4.1. Catalytically active Fe species in the fresh sample

For the fresh sample, several key findings help elucidate the nature of the Fe species, especially under fully hydrated conditions, since our Mössbauer spectroscopic measurements were only conducted on ambient samples. NH_3 TPD results shown in Fig. 2(b) demonstrate that an Fe/H ratio of ~1 was achieved during ion exchange (i.e., each Fe^{2+} ion replaces one H^+). From the Mössbauer spectra shown in Fig. 3, it is concluded that: (1) in its fully hydrated form, Fe(III) dominates in the fresh, calcined sample; and (2) Fe ion species most likely reside in extra-framework (ion exchange) sites (i.e., coordination numbers higher than tetrahedral coordination). A few candidates for these ionic Fe species are plausible and reasonable based on these experimental findings: a hydrated monoferric species ($[Fe(OH)_2]^+$) and a hydrated diferric species ($[HO—Fe—O—Fe—OH]^{2+}$); the latter has been frequently proposed as a key diferric catalytic center in Fe/Zeolites [11,17,25,41,42]. The fact that Fe(III)-RT-2 (Fig. 3(a)) has a high QS (1.86 mm/s) strongly suggests that $[HO—Fe—O—Fe—OH]^{2+}$ is indeed the diferric species present in this material [25]. Fe(III)-RT-1 has a QS = 0.84 mm/s, making a definitive assignment more difficult. We tentatively suggest that this species is $[Fe(OH)_2]^+$, based on the considerations that: (1) for conditions when two framework negative charges are far apart, an $[Fe(OH)2]^+$ species that only balances one negative charge can gain extra stability; and (2) Fe dimers tend to hydrolyze to monomers under fully hydrated conditions [26].
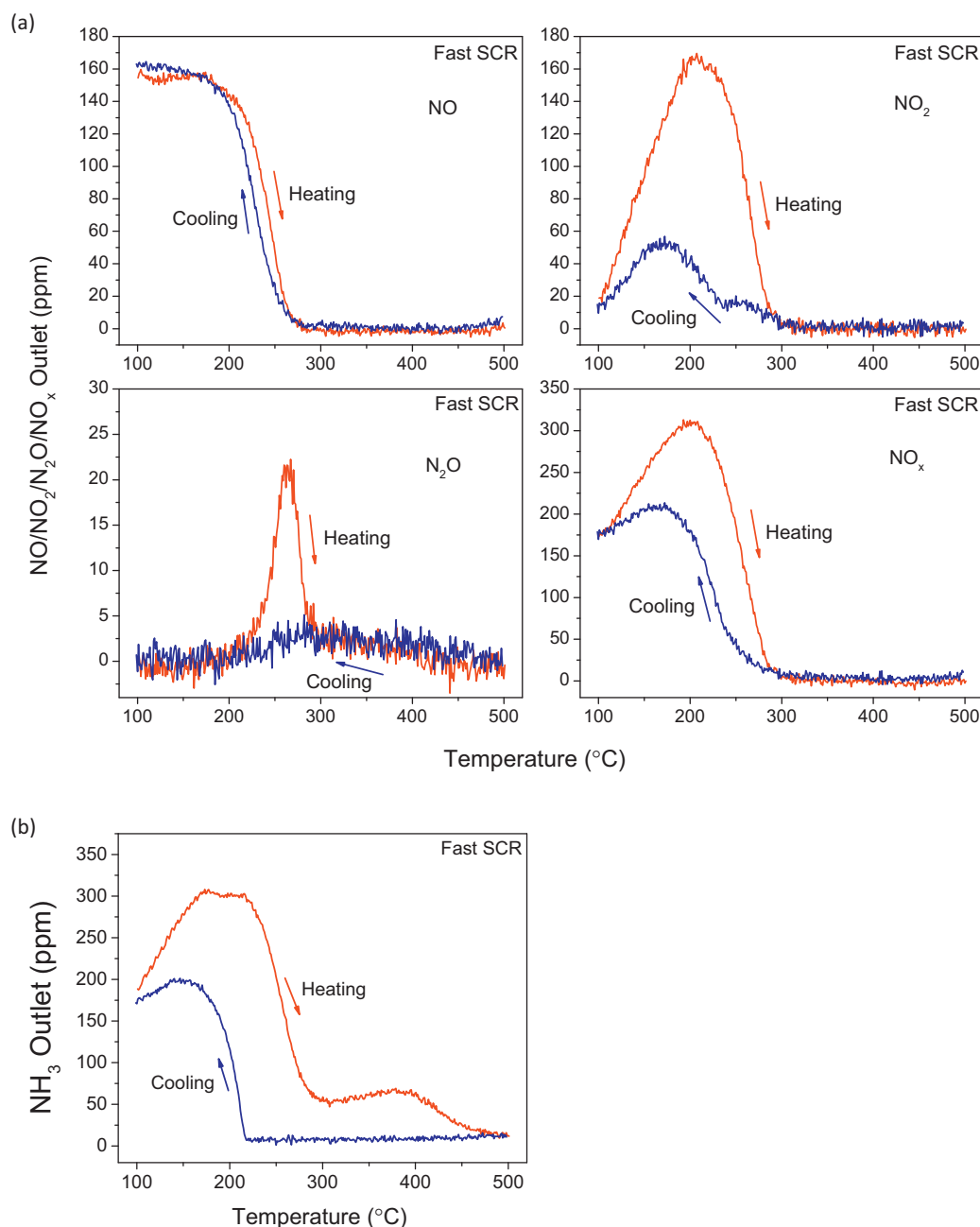
Fig. 12. NO_x (including NO, NO_2, N_2O and total NO_x) (a) and NH_3 (b) outlets during temperature-programmed fast NH_3 − SCR reaction on the fresh Fe/SSZ-13 sample. Reactant feed contains 175 ppm NO, 175 ppm NO_2, 350 ppm NH_3, 14% O_2, 2.5% H_2O balanced with N_2 at a GHSV of 200,000 h^{-1}. The sample is exposed to the feed at 100 °C for 1 h and ramped to 500 °C at 2 °C/min, and then ramped from 500 to 100 °C at 2 °C/min, and maintained at 100 °C for 1 h before finish.

However, we cannot completely rule out a diferric μ–hydroxo complexes (e.g., [HO—Fe—(μ-OH)$_2$—Fe—OH]$^{2+}$) which also typically has a QS < 1 mm/s [24].

From NO/NH_3 oxidation and standard/fast NH_3-SCR reaction results, more details regarding Fe catalytic centers can be derived. Note that H_2O inhibition of these reactions has been repeatedly found during SCR-related reactions [43–45] and, in the present study, results shown in Figs. 3 and 4 clearly demonstrate that H_2O inhibits both NO and NH_3 oxidation reactions. It is important to note that, for NH_3 oxidation and SCR reactions, even if they are carried out under 'dry' conditions H_2O (as a reaction product) can never be totally eliminated from the reaction system. In this case, a catalyst fully dehydrated prior to reactions can become (at least partially) rehydrated. However, this is not the case for NO oxidation where

a catalyst dehydrated prior to reaction should remain dehydrated. With regard to the nature of H_2O inhibition, two scenarios can be envisioned: (1) H_2O alters the nature of the catalytically active centers, and (2) H_2O competes with reactants for the same catalytically active centers. From the NO oxidation results shown in Fig. 7(a), the fresh dehydrated catalyst is extremely active in NO oxidation under 'dry' reaction conditions, yet becomes much less active when H_2O is present. Although the two scenarios discussed above may both play a role in this inhibition, it seems more likely that dehydrated Fe centers are much more active in catalyzing oxidation reactions. In contrast, the H_2O inhibition during NH_3 oxidation displayed in Fig. 8(a) appears to be better rationalized by H_2O competition with NH_3 for Fe sites since the lineshapes for the two light-off curves are very similar.
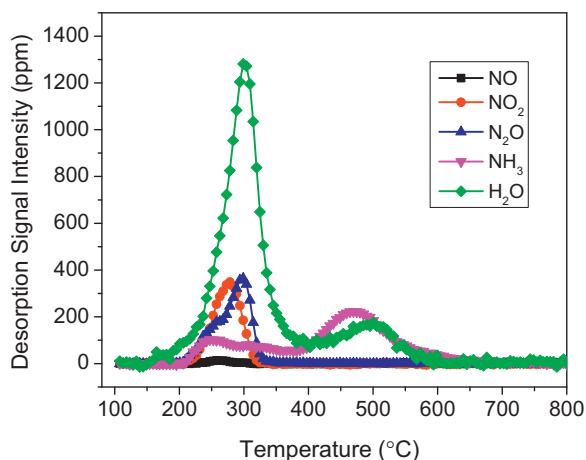
Fig. 13. Temperature-programmed desorption (TPD) of species adsorbed on the fresh Fe/SSZ-13 sample after the temperature-programmed fast SCR reaction step described in Fig. 12. Prior to TPD, the sample is purged with N_2 for 1 h at 100 °C, and then ramped from 100 to 800 °C at 10 °C/min.

Another piece of evidence strongly suggesting that Fe sites are hydrated under 'wet' NH_3 oxidation and NH_3-SCR reactions comes from TPD measurements after reaction. For example, after standard SCR, TPD displayed in Fig. 11 reveals high-temperature H_2O desorption from ~300 to 550 °C. Note that control experiment using H/SSZ-13 fails to result in any H_2O desorption at such temperatures (data not shown). Quantification of the amount of H_2O desorption in this temperature range reveals that it is roughly 2 times of the total Fe content of the sample. Although the H_2O/Fe ratio of ~2 is likely fortuitous, these results are good evidence that the high-temperature H_2O desorption is due to Fe center dehydration. This, in turn, demonstrates that, under 'wet' NH_3 oxidation and NH_3-SCR reaction conditions, the Fe catalytic centers are indeed hydrated.

Following the discussions above, the NH_3-SCR results displayed in Fig. 9(a) can now be better understood. Below ~300 °C, higher NO_x conversions in the absence of H_2O in the reactant feed can be explained in two ways: (1) less competition by H_2O for active sites; and (2) contribution from the fast SCR pathway since NO oxidation to NO_2 becomes facile in the absence of H_2O. Note that temperature-programmed reaction results shown in Figs. 10 and 12 clearly demonstrate that fast SCR proceeds more rapidly than standard SCR below 300 °C (more strictly, this is true only in the absence of severe NH_4NO_3 inhibition, a situation satisfied during our temperature-programmed reaction experiments). Above ~300 °C, lower NO_x conversions under 'dry' reaction conditions are otherwise explained by the fact that (partially) dehydrated Fe active centers are more active in oxidation reactions, thus causing SCR selectivities to decrease. Although direct spectroscopic evidence for the two prototypical hydrated mono- and diferric Fe(III) species discussed above (i.e., $Fe(OH)_2^+$ and $[HO-Fe-O-Fe-OH]^{2+}$) is lacking, the dehydrated counterparts are FeO^+ and $[-O-Fe-\square-Fe-O-]^{2+}$, where "$\square$" is an oxygen vacancy. These latter moieties are expected to be highly active in oxidation reactions. Note that the fresh sample also contains small amounts of FeO_x species and weakly-bound Fe^{2+} (Fig. 3(b)). These moieties, however, are not expected to contribute substantially to any of the reactions described above.

4.2. Effects of hydrothermal aging (HTA)

Hydrothermal stability is a key criterion for diesel engine exhaust aftertreatment catalysts since the catalytic system periodically experiences elevated temperatures (up to ~700 °C) during, for example, particulate filter regeneration. In the present study, a harsh hydrothermal aging treatment (i.e., at 800 °C for 16 h in the presence of H_2O) was performed on our Fe/SSZ-13 catalyst. The XRD patterns shown in Fig. 1 and the BET surface areas/pore volumes displayed in Table 1 demonstrate that the Chabazite zeolite structure is fully maintained following our HTA treatment. However, the ^{27}Al NMR and NH_3-TPD results displayed in Fig. 2 suggest significant dealumination during HTA. In this case, the majority of Fe species are no longer expected to remain in their original charge-balancing sites.

As shown in Fig. 4(a), simulation of the ambient temperature Mössbauer spectrum fails to provide detailed assignments. Still, the QS value of 1.35 mm/s may suggest that the majority of Fe is in an environment close to that of an μ-oxo diferric species [24,25]. A spectrum collected at 77 K (Fig. 4(b)) does allow us to conclude that the predominant Fe species (89%) are not FeO_x cluster species, since the latter gives a sextet spectrum (7%). Therefore, these species are likely highly disordered ferric oxide species, or ferric aluminate. Fortunately, CO/NO titration FTIR provides an alternative way of elucidating the nature of Fe species in the HTA sample. Note that during vacuum annealing of the catalysts prior to the IR measurements, these ferric moieties convert to ferrous moieties via "autoreduction". By comparing CO vibrational spectra for the fresh and HTA samples displayed in Fig. 5(a) and (b), it is evident that the HTA sample has a distinct ν_{CO} band at 2138 cm^{-1}. Note first that this band is more likely ν_{CO} from a Fe^{2+}−CO adduct rather than an OH−CO adduct. This follows since back-donation from OH to CO in OH−CO is highly unlikely so that ν_{CO} of an OH−CO adduct is only found at frequencies higher than physisorbed CO (at ~2142 cm^{-1}) [28,29]. Furthermore, the 2138 cm^{-1} band develops only at relatively high CO pressures indicating weaker interactions between CO and the corresponding Fe^{2+} sites, as compared to the 2196–2193 cm^{-1} band assigned to CO adsorbed on Fe^{2+} remaining at extra-framework cationic sites. Presumably, Fe^{2+} sites that give rise to the 2138 cm^{-1} CO band are heavily shielded by oxygen, a situation fully expected for Fe aluminates and disordered FeO_x species.

NO FTIR spectra shown in Fig. 6 provide additional information on the nature of Fe species in the fresh and HTA samples. For the fresh sample, mono-, di- and tri-nitrosyl species sequentially develop during NO adsorption (Fig. 6(a)), and disappear in a reversed fashion during NO desorption (Fig. 6(b)), as expected. For the HTA sample, two new ν_{NO} bands are found. An 1875 cm^{-1} band develops immediately upon NO introduction and becomes a shoulder peak at high NO pressures. At relatively high NO pressures, another band develops at ~1868 cm^{-1} and gradually shifts to ~1850 cm^{-1} as NO pressures rise. In line with the assignments made by Mul et al. [33] following NO adsorption on steam-treated Fe/MFI catalysts, we assign the 1875 cm^{-1} band to NO adsorbed on iron aluminate species (i.e., $Fe^{II}AlO_x$−NO) and the 1868-1850 cm^{-1} band to NO adsorbed on iron oxide species (i.e., $(Fe^{II}O)_n$−NO). Note again that the iron oxide species must be highly disordered since Mössbauer fails to detect an increase in iron oxide species that give rise to a sextet pattern.

In summary, FTIR results for both CO and NO appear to support the conclusion that upon hydrothermal aging, at least some extra-framework mono- and dimeric ferric ions convert to iron aluminate and disordered iron oxide species. Although during HTA treatment dealumination is very extensive as evidenced from ^{27}Al NMR and NH_3-TPD (Fig. 2); it is not complete since some CO/NO adsorption on extra-frame cationic Fe(II) remains. Therefore, some mono- and dimeric ferric ions remain cationic sites in the HTA sample. In view of the structure-function relationships, a comparison between the fresh and the HTA samples in SCR (Fig. 9(a) and (b)) demonstrates that the $FeAlO_x$ and disordered FeO_x species formed during HTA lack low-temperature activity as compared with mono- and dimeric iron cationic centers in the fresh sample, although at temperatures above ~400 °C, the HTA sample nevertheless displays

significant SCR activity. Furthermore, these species appear to be much less active in oxidation reactions (Figs. 7 and 8); this, in turn, renders the HTA sample even slightly more selective for SCR. Note that these conclusions are consistent with a general understanding regarding the active sites in Fe/zeolite catalysts; that is, certain Fe species are more active at lower temperatures (dimers have been suggested to have higher intrinsic activity than mononuclear sites [46]) although, as reaction temperatures become sufficiently high, all Fe species are active [6,46]. However, due to the continued presence of some charge-balancing Fe cationic species in the HTA sample, we cannot rule out that the majority of activity is still due to these latter sites, whereas FeAlO$_x$ and FeO$_x$ clusters provide limited reactivity even at high reaction temperatures.

4.3. Potential applications for Fe-SSZ-13

Despite rather extensive dealumination, our Fe/SSZ-13 sample maintains structural integrity under extremely severe hydrothermal aging. In this sense, it can certainly be applied as a diesel engine exhaust aftertreatment catalyst. However, since Fe/zeolites lack low-temperature activity as compared with Cu/zeolites, we suggest that Fe/SSZ-13 should be used as a co-catalyst together with Cu/CHA. As is already known, Cu/CHA catalysts provide more limited reactivity and selectivity above ~400 °C after hydrothermal aging [39] while, in the present study, we show that Fe-SSZ-13 maintains good performance. An extra benefit for an Fe/SSZ-13 co-catalyst is its apparently low N$_2$O selectivity. Even under fast-SCR conditions, we show in Fig. 12(a) that N$_2$O outlet concentrations are essentially absent above ~300 °C for our reaction conditions. This can perhaps be explained by the fact that Fe/zeolites are good catalysts for N$_2$O decomposition, and/or N$_2$O-SCR [47–49]. Aged Cu/CHA catalysts do generate significant amounts of N$_2$O above ~400 °C. In this case, an Fe/SSZ-13 co-catalyst might be expected to consume N$_2$O generated by Cu/CHA and, thus, significantly reduce overall N$_2$O emissions for HTA catalyst systems.

5. Conclusions

(1) Using a traditional aqueous solution ion-exchange method under the protection of N$_2$, an Fe/SSZ-13 catalyst active in NH$_3$-SCR is successfully synthesized, thus demonstrating that the small pore CHA structure does not impede Fe^{2+} ion exchange.

(2) Mössbauer and FTIR spectroscopies are utilized to probe the nature of the Fe sites. In the fresh sample, the majority of Fe species are extra-framework cations. Even though their precise stoichiometries and locations are not known, the prototypical monomeric and dimeric ferric ions in hydrated forms are [Fe(OH)$_2$]$^+$ and [HO—Fe—O—Fe—OH]$^{2+}$. Upon dehydration, these convert to [FeO]$^+$ and [—O—Fe—□—Fe—O—]$^{2+}$. These moieties undergo "autoreduction" during vacuum annealing to convert to ferrous species that are probed with CO/NO FTIR titrations. During the severe hydrothermal aging applied in this study, the majority of cationic Fe species convert to FeAlO$_x$ and FeO$_x$ species accompanying considerable dealumination of the framework. The FeO$_x$ species do not give a sextet Mössbauer spectrum, indicating that these are highly disordered. However, some extra-framework cationic Fe species remain during aging.

(3) NO/NH$_3$ oxidation reaction tests reveal that cationic Fe species in dehydrated forms are substantially more active in oxidation reactions. H$_2$O inhibition to oxidation reactions can have two causes: H$_2$O alters the nature of catalytic active species, and/or H$_2$O competes with reactants for active sites. For NH$_3$-SCR, enhancement of NO oxidation under 'dry' conditions promotes NO$_x$ conversions below ~300 °C. This is due mainly to contributions from the fast SCR channel. Above ~300 °C, enhancement

of NH$_3$ oxidation under 'dry' conditions, however, becomes detrimental to NO$_x$ conversions. The HTA sample loses much of the SCR activity below ~300 °C, while above ~400 °C, much of the activity remains. This may suggest that the FeAlO$_x$ and FeO$_x$ cluster species are only active at such elevated temperatures. Alternatively, the high-temperature activity may still be maintained by the remaining extra-framework cationic species.

(4) Even with extremely severe hydrothermal aging, Fe/SSZ-13 maintains structural integrity and much of the SCR activities above ~400 °C. These characteristics make it a good candidate as a catalyst for diesel engine exhaust aftertreatment. However, Fe/SSZ-13 lacks low-temperature activity. We propose that a good solution would be to use Fe/SSZ-13 as a co-catalyst with Cu/CHA. In this way, both low- and high-temperature SCR activity/selectivity maintain. Furthermore, Fe/SSZ-13 may help to decrease N$_2$O release.

References

[1] E. Fridell, M. Skoglundh, B. Westerberg, S. Johansson, G. Smedler, J. Catal. 183 (1999) 196–209.
[2] W.S. Epling, L.E. Campbell, A. Yezerets, N.W. Currier, J.E. Parks, Catal. Rev. 46 (2004) 163–245.
[3] S. Roy, A. Baiker, Chem. Rev. 109 (2009) 4054–4091.
[4] G. Centi, S. Perathoner, Appl. Catal. A 132 (1995) 179–259.
[5] V.I. Pârvulescu, P. Grange, B. Delmon, Catal. Today 46 (1998) 233–316.
[6] S. Brandenberger, O. Krocher, A. Tissler, R. Althoff, Catal. Rev. 50 (2008) 492–531.
[7] I. Bull, W.M., Xue, P., Burk, R.S., Boorse, W.M., Jaglowski, G.S., Koermer, A., Moini, J.A., Patchett, J.C., Dettling, M.T., Caudle, US Patent, 2009, US7601662 B2.
[8] J. Andersen, J.E., Bailie, J.L., Casci, H.Y., Chen, J.M., Fedeyko, R.K.S., Foo, R.R., Rajaram, International Patent, 2008,WO/2008/132452.
[9] U. Deka, I. Lezcano-Gonzalez, B.M. Weckhuysen, A.M. Beale, ACS Catal. 3 (2013) 413–427.
[10] F. Gao, J.H. Kwak, J. Szanyi, C.H.F. Peden, Top. Catal. 56 (2013) 1441–1459.
[11] T.V. Voskoboinikov, H.Y. Chen, W.M.H. Sachtler, Appl. Catal. B 19 (1998) 279–287.
[12] M.S. Kumar, M. Schwidder, W. Grünert, A. Brückner, J. Catal. 227 (2004) 384–397.
[13] M.S. Kumar, M. Schwidder, W. Grünert, U. Bentrup, A. Brückner, J. Catal. 239 (2004) 173–186.
[14] M. Schwidder, S. Heikens, A. De Toni, S. Geisler, M. Berndt, A. Brückner, W. Grünert, J. Catal. 259 (2008) 96–103.
[15] U. Deka, A. Juhin, E.A. Eilertsen, H. Emerich, M.A. Green, S.T. Korhonen, B.M. Weckhuysen, A.M. Beale, J. Phys. Chem. C 116 (2012) 4809–4818.
[16] F. Gao, E.D. Walter, E.M. Karp, J.Y. Luo, R.G. Tonkyn, J.H. Kwak, J. Szanyi, C.H.F. Peden, J. Catal. 300 (2013) 20–29.
[17] X.B. Feng, W.K. Hall, J. Catal. 166 (1997) 368–376.
[18] F. Gao, E.D. Walter, N.M. Washton, J. Szanyi, C.H.F. Peden, ACS Catal. 3 (2013) 2083–2093.
[19] J. Szanyi, J.H. Kwak, H.Y. Zhu, C.H.F. Peden, Phys. Chem. Chem. Phys. 15 (2013) 2368–2380.
[20] T.S. Peretyazhko, J.M. Zachara, R.K. Kukkadapu, S.M. Heald, I.V. Kutnyakov, C.T. Resch, B.W. Arey, C.M. Wang, L. Kovarik, J.L. Phillips, D.A. Moore, Geochim. Cosmochim. Acta 92 (2012) 48–66.
[21] J.H. Kwak, D. Tran, S.D. Burton, J. Szanyi, J.H. Lee, C.H.F. Peden, J. Catal. 287 (2012) 203–209.
[22] S. Brandenberger, O. Kröcher, A. Wokaun, A. Tissler, R. Althoff, J. Catal. 268 (2009) 297–306.
[23] R.L. Garten, W.N. Delgass, M. Boudart, J. Catal. 18 (1970) 90–107.

[24] D.M. Kurts Jr., Chem. Rev. 90 (1990) 585–606.
[25] K.A. Dubkov, N.S. Ovanesyan, A.A. Shteinman, E.V. Starokon, G.I. Panov, J. Catal. 207 (2002) 341–352.
[26] W.N. Delgass, R.L. Garten, M. Boudart, J. Phys. Chem. 73 (1969) 2970–2979.
[27] A. Diamant, M. Pasternak, A. Banin, Clay. Clay Miner. 30 (1982) 63–66.
[28] M. Mihaylov, E. Ivanova, N. Drenchev, K. Hadjiivanov, J. Phys. Chem. C 114 (2010) 1004–1014.
[29] J. Kim, A. Jentys, S.M. Maier, J.A. Lercher, J. Phys. Chem. C 117 (2013) 986–993.
[30] L.J. Lobree, I.C. Hwang, J.A. Reimer, A.T. Bell, J. Catal. 186 (1999) 242–253.
[31] R. Kefirov, E. Ivanova, K. Hadjiivanov, S. Dzwigaj, M. Che, Catal. Lett. 125 (2008) 209–214.
[32] L. Benco, T. Bucko, R. Grybos, J. Hafner, Z. Sobalik, J. Dedecek, S. Sklenak, J. Hrusak, J. Phys. Chem. C 111 (2007) 9393–9402.
[33] G. Mul, J. Perez-Ramirez, F. Kapteijn, J.A. Moulijn, Catal. Lett. 80 (2002) 129–138.
[34] M. Rivallan, G. Ricchiardi, S. Bordiga, A. Zecchina, J. Catal. 264 (2009) 104–116.
[35] G. Berlier, G. Spoto, G. Ricchiardi, S. Bordiga, C. Lamberti, A. Zecchina, J. Mol. Catal. A 182–183 (2002) 359–366.
[36] R. Joyner, M. Stockenhuber, J. Phys. Chem. B 103 (1999) 5963–5976.
[37] J.H. Kwak, J.H. Lee, S.D. Burton, A.S. Lipton, C.H.F. Peden, J. Szanyi, Angew. Chem. Int. Ed. 52 (2013) 9985–9989.
[38] A. Grossale, I. Nova, E. Tronconi, Catal. Today 136 (2008) 18–27.
[39] S.J. Schmieg, S.H. Oh, C.H. Kim, D.B. Brown, J.H. Lee, C.H.F. Peden, D.H. Kim, Catal. Today 184 (2012) 252–261.
[40] A. Grossale, I. Nova, E. Tronconi, D. Chatterjee, M. Weibel, J. Catal. 256 (2008) 312–322.
[41] P. Marturano, L. Drozdova, A. Kogelbauer, R. Prins, J. Catal. 192 (2000) 236–247.
[42] P. Sazama, B. Wichterlova, E. Tabor, P. Stastny, N.K. Sathu, Z. Sobalik, J. Dedecek, S. Sklenak, P. Klein, A. Vondrova, J. Catal. 312 (2014) 123–138.
[43] O. Krocher, M., Devadas, M., Elsener, A., Wokaun, N., Soger, M., Pfeifer, Y., Demel, L. Mussmann, Appl. Catal. B 66, 2006, 208-216.
[44] P.S. Metkar, N. Salazar, R. Muncrief, V. Balakotaiah, M.P. Harold, Appl. Catal. B 104 (2011) 110–126.
[45] M.P. Ruggeri, I. Nova, E. Tronconi, Top. Catal. 56 (2013) 109–113.
[46] M. Schwidder, M.S. Kumar, K. Klementiev, M.M. Pohl, A. Bruckner, W. Grunert, J. Catal. 231 (2005) 314–330.
[47] B. Coq, M. Mauvezin, G. Delahay, J.B. Butet, S. Kieger, Appl. Catal. B 27 (2000) 193–198.
[48] J. Perez-Ramirez, F. Kapteijn, J.C. Groen, A. Domenech, G. Mul, J.A. Moulijn, J. Catal. 214 (2003) 33–45.
[49] J. Perez-Ramirez, F. Kapteijn, G. Mul, J.A. Moulijn, J. Catal. 208 (2002) 211–223.